J Nanopart Res (2019) 21: 231
https://doi.org/10.1007/s11051-019-4688-x

RESEARCH PAPER

Macrophage-targeted and clearable glutathione-based MRI nanoprobes for atherosclerosis molecular imaging

Liang Li · Jiahui Wang · Menglin Wu · Yana He · Hongtuan Zhang · Guoping Xu · Li Chen · Xinying Jia · Qi Guo · Xuening Zhang

Received: 6 May 2019 / Accepted: 14 October 2019 / Published online: 7 November 2019

Abstract Foam macrophage infiltration is one of the clinical features of high-risk atherosclerotic plaques. Many imaging modalities such as magnetic resonance imaging (MRI) have been used to detect foam macrophages for evaluating plaque vulnerability. However, targeting efficiency, biocompatibility, and clearance remain pivotal challenges in design of new MRI contrast agents. Herein, we report a sensitive, class AI scavenger receptors (SR-AI)-targeted, glutathione-biomineralized gadolinium-based nanoparticle for noninvasive precise MR imaging of macrophages within carotid atherosclerotic lesions in apoE-deficient ($ApoE^{-/-}$) mice. The resultant PP1 (16-mer peptide, LSLERFLRCWSDAPAK)-gold-gadolinium nanoparticles (NPs) possessed superior stability, prominent longitudinal relaxivity, and negligible cytotoxicity. In vitro results showed the highest internalization in activated macrophages and in vivo MR images revealed signal augment in carotid atherosclerotic lesions after PP1-gold-gadolinium NP administration at 4 h and 12 h, which were strong testimonial to the formidable macrophage-targeting ability and the subsequent atherosclerosis-retention biofunctions. To summarize, our tactically elaborated biocompatible multifunctional MR NPs integrate T1 signal amplification, precise macrophage targeting, and systematic clearance capabilities, which offer an innovative strategy for noninvasively characterizing vulnerable plaques of early-stage atherosclerosis, or for a wide range of clinical diagnosis and treatment applications.

Liang Li and Jiahui Wang contributed equally to this work.

Electronic supplementary material The online version of this article (https://doi.org/10.1007/s11051-019-4688-x) contains supplementary material, which is available to authorized users.

L. Li · J. Wang · M. Wu · G. Xu · L. Chen · Q. Guo · X. Zhang (✉)
Department of Radiology, The Second Hospital of Tianjin Medical University, Tianjin, People's Republic of China
e-mail: zhangxuening@tmu.edu.cn

Y. He
Department of Medical Imaging, The First Teaching Hospital of Tianjin University of Traditional Chinese Medicine, Tianjin, People's Republic of China

H. Zhang
Department of Urology, The Second Hospital of Tianjin Medical University, Sex Hormone Research Center, Tianjin Institute of Urology, Tianjin, People's Republic of China

X. Jia
Department of Ultrasonography, Tianjin Medical University General Hospital, Tianjin, People's Republic of China

Keywords Clearable nanoparticles · Macrophage targeting · MRI · Atherosclerosis · Nanomedicine

Introduction

Despite significant diagnostic advances achieved over the past decades, cardiovascular events resulting from atherosclerosis remain the leading cause of mortality worldwide (Nabel and Braunwald 2012; Arbab-Zadeh et al. 2012). Atherosclerosis is a multifactorial systemic disorder characterized by the accumulation of inflammatory cells and lipids on the inner surface of artery walls, resulting in plaques built up gradually (Htun et al. 2017; Yan et al. 2018). Recent insights into the pathogenesis of atherosclerosis indicate that plaque vulnerability is primarily related to plaque composition (Virmani et al. 2006; Wen et al. 2014). Vulnerable plaques with highly inflamed macrophages and large lipid cores are likely to expose the thrombogenic materials of plaque core, ultimately precipitating plaque rupture and serious atherothrombotic events (Ross 1999; Fuster et al. 2005; Dweck et al. 2016). To identify high-risk patients who could benefit from early interventions, developing specific noninvasive methods to accurately characterize plaque composition, monitor rupture-prone vulnerable plaques, and exploit potential translational tools becomes urgent and necessary.

Numerous researches have shown that macrophages are markers of unstable atherosclerotic plaques (Qiao et al. 2017; Kolodgie et al. 2003; Virmani et al. 2006). They highly express SR-AI (Kodama et al. 1990), which mediate internalizing of different forms of modified low-density lipoproteins, promote formation and activation of lipid-laden foam cells, and play a crucial role in atherosclerosis at all stages of the disease development (Suzuki et al. 1997; Hiltunen et al. 1998). The marked overexpression of SR-AI is found in lesional macrophages of advanced atherosclerotic plaques, but not in normal vessel walls (Gough et al. 1999), and is associated with efficient receptor-mediated endocytosis (Winther et al. 2000), rendering SR-AI as a promising molecular target for specific recognition of foam macrophages. The application of selective SR-AI ligands, such as the newly found peptide PP1 (Segers et al. 2012, 2013), as a homing device for contrast agents may hence allow macrophage-targeted in vivo imaging and monitoring of atherosclerotic plaques in general but also give insight into their actual composition and vulnerability.

T1-weighted magnetic resonance imaging (MRI) has emerged as a leading noninvasive diagnostic modality for evaluating plaque composition and assessing plaque burden (Zhou et al. 2015) thanks to its outstanding soft tissue resolution, unlimited tissue penetration depth, and gadolinium (Gd)-based positive contrast agents (Yang et al. 2016; Samira et al. 2011). Unfortunately, traditional small molecular Gd chelates (Caravan et al. 1999; Zhang et al. 2011) are often discouraged by non-specificity, low relaxivity, and fast renal clearance (Zhao et al. 2017; McDonald et al. 2015). To overcome these obstacles, inorganic-based Gd-containing nanoparticles have been explored, taking advantage of passive targeting ability by enhanced permeability and retention (EPR) effect (Yu et al. 2017) compared with small molecular tracers. However, many nanoparticle-based contrast agents have relatively larger hydrodynamic diameters (HDs, typically > 10 nm), which are above the kidney filtration threshold (KFT) of 5.5 nm (Choi et al. 2007). Thus, these nanoparticles prefer to be seriously captured in liver and spleen by the reticuloendothelial system (RES) after administration, which not only reduces the targeting efficiency and specificity but also induces latent toxicity for normal tissues (Chen et al. 2014), impeding their clinical applications. In this regard, developing biocompatible and more efficient Gd-based nanoparticles with proper sizes which have little accumulation in normal tissues while getting adequate doses in plaque locations is critically demanded.

Herein, we report a facile, one-pot strategy by which a Gd-based MRI contrast agent (PP1-gold-gadolinium NPs) was synthesized via biomineralization using human autologous protein glutathione as a template (Scheme 1a). The nanoparticles were functionalized by conjugating PP1 peptide as SR-AI-specific targeting ligand to specifically recognize foam macrophages, favoring in vivo precise MR imaging of vulnerable plaques (Scheme 1b). The surface properties of the nanoparticles were characterized by various physicochemical means. Systematic in vitro and in vivo experiments were designed to carefully evaluate the cellular binding specificity, SR-AI-directed targeting ability, and the pharmacokinetics. Different from the previously reported nanoparticles based on BSA molecules (Le et al. 2016; Hu et al. 2013), our human autologous protein glutathione-based nanoprobes (PP1-gold-gadolinium NPs) with smaller particle size and well-engineered surface chemistry enabled superior penetration and long retention behavior in plaques. More importantly, rapid diffusion followed by effective elimination from normal

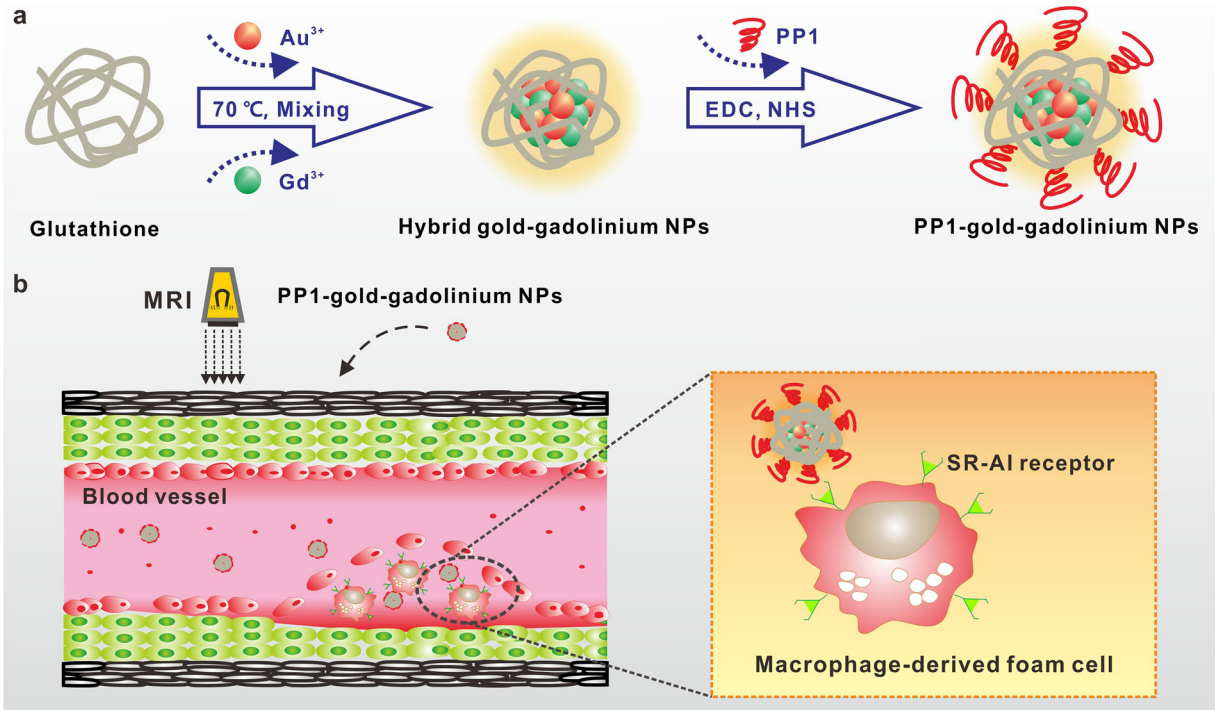

Scheme 1 Schematic illustration of PP1-gold-gadolinium NPs for in vivo MR imaging of vulnerable atherosclerotic plaques. **a** Schematic illustration of the procedure for fabrication of PP1-gold-gadolinium NPs. **b** Targeting mechanism of PP1-gold-gadolinium NPs to specifically recognize macrophage-derived foam cells via SR-AI for MR imaging

tissues rendered PP1-gold-gadolinium NPs as an advanced MRI-positive contrast agent for direct detection of plaques with specificity, efficacy, safety, and promising clinical translational potential.

Materials and methods

Materials

Chloroauric acid ($HAuCl_4$), glutathione (GSH), gadolinium chloride hexahydrate ($GdCl_3 \cdot 6H_2O$), and diethylenetriaminepentaacetic acid (DTPA) were purchased from Sigma-Aldrich (Louis, MO, USA). 1-Ethyl-3-(3-dimethylaminopropyl)-carbodiimide hydrochloride (EDC), *N*-hydroxysuccinimide (NHS), and the peptide PP1 (LSLERFLRCWSDAPAK) were obtained from GL Biochem Co., Ltd. (Shanghai, China). Dulbecco's modified Eagle's medium (DMEM), penicillin-streptomycin, and fetal bovine serum (FBS) were provided by Gibco BRL (Grand Island, NY, USA). 3-(4,5-Dimethylthiazol-2-yl)-2,5-diphenyltetrazolium bromide (MTT) and 4′6-diamidino-2-phenylindole (DAPI) were supplied by Merck (Germany). All initial reagents were used as received without further purification.

Synthesis of PP1-gold-gadolinium NPs

In a typical experiment, the aqueous gadolinium chloride solution (0.5 mL, 500 mM) was mixed with $HAuCl_4$ solution (24 mM, 2.1 mL) under vigorous magnetic stirring in a one-neck flask. Then, GSH solution (1 mg/mL, 25 mL) was added to the mixture and kept on constant stirring for 20 min. After that, NaOH solution (1 M) was introduced dropwise to trigger the reduction capability of the responsible amino acids of GSH. Subsequently, the mixture was continuously stirred overnight to ensure the complete reduction of $HAuCl_4$. The product was purified by centrifugation with the mixture of ethanol and water three times to remove small molecules, including some metal ions and dispersed in phosphate buffer saline (PBS, 0.01 M, pH 7.4) ultimately.

PP1 peptide was conjugated on the surface of the gold-gadolinium NPs according to amide condensation reaction (Deng et al. 2015). The gold-gadolinium NPs (50 mg/mL, 0.1 mL), PP1 (1 mg/mL, 0.01 mL), and

EDC (8 mg/mL, 0.02 mL) were dissolved in PBS and oscillated (100 rpm/min) on a shaker at 37 °C for 2 h. Finally, the resulting conjugates were washed several times via centrifugation and stored in PBS at 4 °C for further study.

Characterizations of PP1-gold-gadolinium NPs

Transmission electron microscopy (TEM) images of the gold-gadolinium NPs and PP1-gold-gadolinium NPs were obtained using a JEOL 100CX transmission electron microscope at a 200-kV operating voltage. The NPs were dispersed in PBS and dried onto the carbon-coated copper grids and the air-dried samples were directly observed by electron microscope. The HDs and zeta potentials were measured on a dynamic light scattering system (JEM Zetasizer Nano ZS90, Malvern Instruments, England, UK) equipped with a 4-mW He-Ne laser (λ = 633 nm) at room temperature. The UV-vis absorption spectra were measured by Shimadzu UV-1700 spectrophotometer. The concentration of Gd:Au was tested by the inductively coupled plasma-atomic emission spectrometry (ICP-AES).

In vitro MR imaging and relaxivity characterization

The T1-weighted MR phantom images of Magnevist, gold-gadolinium NPs, and PP1-gold-gadolinium NP solutions with different Gd concentrations (0, 0.05, 0.15, 0.3, 0.5, 0.75, 1.0 mM) were acquired using a 3.0-T clinical MR scanner (Discovery 750, General Electric Company, USA) with the CUBE T1 sequence. The measurement parameters were as follows: Freq. FOV = 10.0 mm^2, phase FOV = 1.00 mm^2, repetition time (TR) = 400.0 ms, echo time (TE) = minimum, slice thickness = 1.0 mm, spacing = 0.2 mm, slices = 16, matrix acquisition = 192 × 192, NEX = 3. The longitudinal (T1) relaxation times of the NP samples were measured on the aforementioned 3.0-T MR scanner at room temperature with the following parameters: MOLLI T1 mapping sequence, Freq. FOV = 10.0 mm^2; phase FOV = 1.00 mm^2; TR = 4000 ms; TE = 68 ms; slice thickness = 4.0 mm; spacing = 1.0 mm; slices = 17; flip angle = 110°; echo train length (ETL) = 16; inversion time = 200 ms. The 1/T1 relaxation times (s^{-1}) were plotted against Gd concentrations to respectively determine the longitudinal relaxation rates (r_1) of each sample from the slope of the linear fit.

Colloidal and relaxivity stability studies of PP1-gold-gadolinium NPs

The as-prepared PP1-gold-gadolinium NPs were incubated in deionized (DI) water, PBS (0.01 M, pH 7.4) and DMEM (containing 10% FBS) at room temperature. The temporal evolution profiles of HDs and zeta potentials were regularly monitored throughout a storage period of up to 10 weeks to investigate the colloidal stability. Simultaneously, the relaxivity stability was estimated by recording variations in relative MR signal intensities and relaxation times (T1) of the PP1-gold-gadolinium NPs for 10 weeks. The data shown here are for after-incubation nanoparticle samples reconstituted in water by three repeated washings with deionized water via centrifugation to remove excess of biomolecules.

Cell culture and cytotoxicity assays

The murine macrophage cells (RAW264.7) and normal human kidney cell lines (293 T) were cultured in DMEM supplemented with 10% FBS and 1% penicillin-streptomycin. The cultured cells were maintained at 37 °C with 5% CO_2 atmosphere and 90% relative humidity in 96-well plates at 1 × 10^4 cells per well. After the cells reached 60–80% confluence, they were incubated with gold-gadolinium NPs or PP1-gold-gadolinium NPs (0, 10, 25, 50, 75, 150, 300, and 600 μg/mL) to evaluate the cytotoxic effect of NPs by MTT assay. After 24 h or 48 h of incubation, 100 μL of fresh medium and 10 μL of MTT solution (5 mg/mL in sterile PBS) were added to each well and cultured for an additional 4 h. After removal of the old medium, 150 μL of dimethyl sulfoxide (DMSO) was added to each well to dissolve the formazan produced by living cells. The plates were then gently shaken, and the absorbance at 490 nm of each well was measured using a multifunctional microplate reader to calculate relative cell viabilities.

In vitro cellular binding specificity and MR imaging

RAW264.7 macrophage, a murine cell line, overexpresses SR-AI after being stimulated by human Ox-LDL (Wen et al. 2014). To investigate

whether PP1-gold-gadolinium NPs could specifically target SR-AI receptor, the cell fluorescence and MR imaging in vitro were performed on RAW264.7 macrophages under two conditions: preincubation with/without human Ox-LDL (100 μg/mL) for 24 h. For confocal imaging, RAW264.7 cells were seeded in confocal dishes at a density of 2×10^4 cells/dish, incubated for 24 h under the abovementioned conditions, and fixed with 4% paraformaldehyde. Then, the cells were treated with Cy5-labeled gold-gadolinium NPs, PP1-gold-gadolinium NPs, or excess PP1 (30 μg/mL) plus PP1-gold-gadolinium NPs at the concentration of 0.6 mg/mL for 4 h, washed with PBS 3 times and stained with DAPI (500 ng/mL) for 15 min. Then, samples were visualized on a confocal microscope (Olympus FV10i, Tokyo, Japan).

For in vitro MR imaging, the two different states of RAW264.7 macrophages were also treated with various NPs at 37 °C for 4 h. The cells were then washed three times with PBS and harvested by trypsinization for 3 min. After centrifugation at 1000 rpm for 3 min, cells were resuspended in 100 μL PBS in Eppendorf tubes (Axygen, CA, USA). T1-weighted MR imaging was carried out with the aforementioned 3.0-T MR scanner using the CUBE T1-weighted sequence (TR = 400 ms, TE = 35 ms, slice = 12, slice thickness = 0.8 mm, matrix = 256 × 256). Further on, MR imaging of human Ox-LDL-preconditioned macrophages incubated with different concentrations of PP1-gold-gadolinium NPs for different incubation times was also performed.

In vivo MR imaging of ApoE$^{-/-}$ mice with atherosclerotic lesions

Eight-week-old female apolipoprotein E-deficient (ApoE$^{-/-}$) mice were purchased from the Vital River Laboratory Animal Technology Co., Ltd., Beijing. Mice were fed with a high-fat diet (HFD, western-type diet containing 15% butterfat and 0.25% cholesterol) for 2 weeks prior to surgery. Subsequently, mice were deeply anesthetized with 5% chloral hydrate (6 mL/kg), and a rigid polyethylene perivascular cast was placed around the left carotid artery. Then, the entry wounds were closed, and the mice were returned to cages and kept on the HFD for another 16 weeks. All animal studies were performed in compliance with the Care and Use of Laboratory Animals formulated by the National Society for Medical Research and all experiments were conducted in accordance with the Helsinki declaration.

In vivo MR imaging was performed on a 3.0-T MR scanner using a small-animal coil after mice were anesthetized with 5% chloral hydrate. MR images were acquired preceding NP administration as well as at 4 h and 12 h following tail vein injection of 200 mg/kg body weight NPs. For the in vivo competitive inhibition group, ApoE$^{-/-}$ mice received intravenous injection of a mixture of 0.5 mg free PP1 peptide and 200 mg/kg body weight PP1-gold-gadolinium NPs. For in vivo imaging, a T1 FSE sequence was used (Freq. FOV = 10.0 mm^2, phase FOV = 1.00 mm^2, TR = 800 ms, TE = Min Full, slice thickness = 1.0 mm, spacing = 0.2 mm, slices = 22, matrix = 256 × 256, NEX = 4) to scrutinize the atherosclerotic lesions.

Pre-, 4-h, and 12-h post-NP injection MR images were measured using MedExplorer software. The carotid wall was identified and signal intensities of regions of interest (ROIs) were analyzed by two independent observers who were blinded to the types of NPs and histopathological data. Contrast to noise ratio (CNR) of each ROI was determined by the average signal intensity corrected on the standard deviation of the noise level (Wang et al. 2016a, b). The normalized MR signal enhancements were plotted as a percentage increase in average CNR over time using the following equation: $(CNR_{post} - CNR_{pre}) / CNR_{pre} \times 100\%$. CNR_{pre} was calculated from images before NP administration, and CNR_{post} represented the CNR value obtained after NP injection.

Histopathology and immunohistochemistry

Carotid artery segments aligned to the MR imaged region were excised, aliquoted into 5-mm segments, frozen in optimal cutting temperature (OCT) compound and sectioned (4 μm). The obtained transverse sections were stained with silver-staining and Oil Red O for the recognition of deposition of NPs and neutral lipids (triglycerides and cholesterol esters) (Qiao et al. 2017). Immunohistochemical staining was performed to further analyze the histology and the expression of SR-AI in the carotid wall, and a macrophage-specific marker F4/80 protein was used to identify the lesional macrophages (Segers et al. 2013). Light hematoxylin counterstaining was applied to visualize all nuclei in tissue sections. All microscopic images were processed under a light microscope (Olympus, Tokyo, Japan) with independent pathologists.

In vivo blood circulation behavior and biodistribution studies

In this study, 200 μL of PP1-gold-gadolinium NPs were intravenously injected into ApoE$^{-/-}$ mice via tail vein at a dose of 20 mg/kg. For the blood circulation analysis, serial blood samples were collected from the eye socket at indicated time points (1 min, 5 min, 15 min, 30 min, 1 h, 2 h, 4 h, 8 h, 16 h, and 24 h), followed by weighed and dissolved in digestive chloroazotic acid (V_{HCl}/V_{HNO3} = 1/3) to determine the amount of gadolinium and gold in the blood using ICP-MS. For the biodistribution analysis, mice were sacrificed at varying i.v. time points (24 h, 3 days, and 7 days), and the major organs (heart, liver, spleen, lung, kidney, stomach, intestine, muscle, fat, bone marrow, lymph) and excrements (bile, feces, and urine) were collected, weighed, and digested in aqua regia (6 mL, V_{HCl}/V_{HNO3} = 1/3) overnight. The solutions were placed on a heating plate to volatilize the acid components and then diluted to 10 mL with free deionized water. Then, gadolinium and gold contents of the samples were measured by ICP-MS.

In vivo biosafety evaluation

A total of 30 mg/mL PP1-gold-gadolinium NPs was used for the biosafety evaluation experiment via intravenous injection, and the concentration was up to 600 mg/kg in the ApoE$^{-/-}$ mice. At everyday time points after administration, mice were weighed and assessed for behavioral changes. By a standard saphenous vein sampling, blood was drawn for standard hematology analysis and biochemistry tests. Mice treated with PBS were used as the blank control. Upon the completion of blood collection, mice were sacrificed, and major organs (heart, liver, spleen, lung, and kidney) were harvested, fixed using 4% paraformaldehyde, embedded into paraffin, sliced (4 μm), and stained with hematoxylin and eosin (H&E) for morphometric analysis. All of the biopsy samples were examined by an optical microscope.

Results and discussion

Fabrication and characterization of PP1-gold-gadolinium NPs

In this work, the gold-gadolinium NPs were prepared according to a facile bioinspired synthetic route (Scheme 1a). GSH, possessing strong affinity for metal atoms and reducibility under alkaline conditions (Luo et al. 2012), was employed as the template protein for biomineralization. Upon adding $HAuCl_4$ and $GdCl_3$ to the aqueous GSH solution and adjusting the pH to alkalinity, Au^{3+} ions immediately reacted with the thiol group to form stable Au^{+}-GSH complex owing to strong Au^{+}-S interaction. Contemporaneously, Gd^{3+} were formed as Gd^{3+}-GSH intermediates employing the chelation and electrostatic interaction with the carboxylic group. In alkaline environment, more and more Au^{3+} ions were further reduced and compactly aggregated on Au^{+}-GSH complex; meanwhile, the Gd^{3+}-GSH intermediates transformed from chelated ions to oxide state. At present, the gold-gadolinium NPs with regular ordered structure were prepared. Compared with previous reports by Hu et al. (2013), the method developed in this study simplified the synthetic procedures, shortened the reaction time, and reduced the cost. As a result, the mass production of such contrast agents could be easily scaled up by the environmentally benign and reproducible process. PP1 antibody was then conjugated using EDC, by which the reduction capability of responsible amino acids in GSH was triggered and PP1 were consequently conjugated.

Gold-gadolinium NPs and PP1-gold-gadolinium NPs were well dispersed in PBS solution and exhibited typical spherical morphology as characterized by TEM (Fig. 1a, b) and HRTEM (Fig. S1). EDS analysis (Fig. S2) demonstrated the Au/Gd ratio within gold-gadolinium NPs was about 1.12:1. Meanwhile, the elemental mapping (Fig. S3) further confirmed the composition and homogeneous distribution of Au and Gd elements. Dynamic light scattering indicated the HDs of PP1-gold-gadolinium NPs were 5.50 ± 0.36 nm (Fig. 1c), a bit larger than that of gold-gadolinium NPs (3.0 nm) due to PP1 antibody decoration. Compared with previous reports using similar synthesis routes (Le et al. 2016), our prepared PP1-gold-gadolinium NPs have an ultrasmall particle size, which is in favor of penetration into lesion site and renal excretion from body. The Gd element contents of gold-gadolinium NPs and PP1-gold-gadolinium NPs were further measured by ICP-AES, and the atomic ratios between Gd and Au elements were 0.97:1 and 1.125:1, respectively, providing powerful guarantee for tracing their bio-behaviors by T1 MR imaging based on Gd. The surface modification was confirmed by Fourier transform infrared (FTIR) spectra. As in Fig. 1d, compared with unmodified gold-gadolinium NPs, FTIR spectrum of PP1-gold-

gadolinium NPs displayed the characteristic peaks corresponding to –CO–NH– (1521 cm^{-1}) and –COC– (1087 cm^{-1}), indicating PP1 peptide was triumphantly grafted. Zeta potentials of gold-gadolinium NPs and PP1-gold-gadolinium NPs were changed from − 10.2 to − 19.3 mV (Fig. S4), providing further evidence for successful peptide conjugation. In addition, the UV-vis spectra (Fig. 1e) exhibited a distinct peak at 400 nm, which matched with GSH-protected Au bioconjugates reported by Luo et al. (2012).

In vitro MR imaging properties

To illustrate MR enhancement capacity of PP1-gold-gadolinium NPs, T1-weighted images of dispersions of gold-gadolinium NPs, PP1-gold-gadolinium NPs, and Magnevist at various Gd concentrations were captured using a 3.0-T MR scanner. As shown in Fig. 2a, b, the as-synthesized NPs generated bright signals on T1-weighted images and exhibited concentration-dependent positive enhancement effect. When Gd concentration was 1.0 mM, PP1-gold-gadolinium NPs exhibited excellent MR signals, markedly superior to Magnevist, the clinically approved T1 contrast agent (Fig. S5). T1 relaxation rates (1/T1) of probes were found to have a linear relationship with Gd concentrations. The longitudinal relaxivities (r_1) of gold-gadolinium NPs and PP1-gold-gadolinium NPs were 20.5 mM^{-1} s^{-1} and 24.0 mM^{-1} s^{-1}, respectively, which were almost five times higher compared with the clinically used Magnevist (r_1 = 4.8 mM^{-1} s^{-1}, Fig. 2c). The appealing MR enhancement ability of NPs might be due to the confined tumbling of Gd^{3+} in the biomacromolecule, resulting in longer rotational correlation time (Zhou et al. 2015). In addition to the improved r_1 values, the transverse relaxivity (r_2) of PP1-gold-gadolinium NPs (r_2 = 23.050 mM^{-1} s^{-1}) was also significantly higher than that of Magnevist (r_2 = 5.114 mM^{-1} s^{-1}; Fig. S6). The relatively low r_2/r_1 ratio (r_2/r_1 ratio = 0.96 < 3) of PP1-gold-gadolinium NPs is beneficial to produce a desired

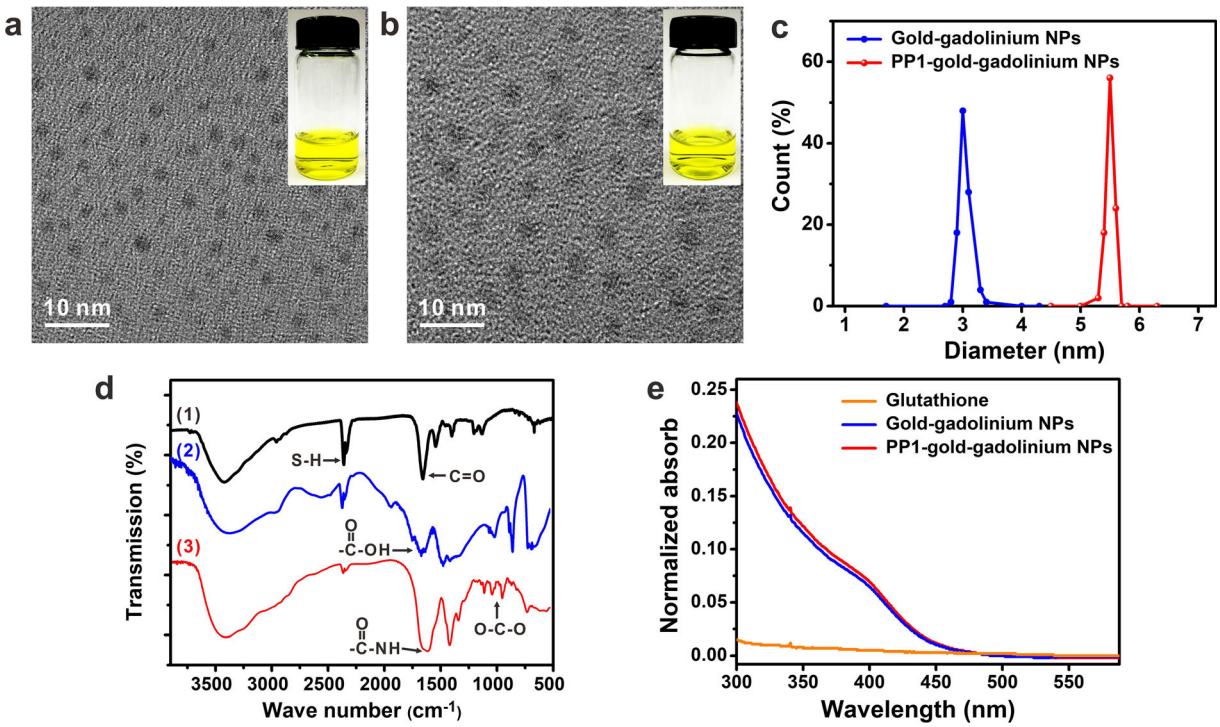

Fig. 1 Characterizations of the main physicochemical properties of the nanoparticles. **a** TEM images of Gold-gadolinium NPs and **b** PP1-gold-gadolinium NPs. Upper inserts show photographs of the NPs dispersed in PBS. **c** The number size distribution of the as-prepared gold-gadolinium NPs and PP1-gold-gadolinium NPs. **d** FTIR spectra of (1) pure PP1, (2) gold-gadolinium NPs, and (3) PP1-gold-gadolinium NPs. **e** UV-vis spectra of pure GSH, gold-gadolinium NPs, and PP1-gold-gadolinium NPs

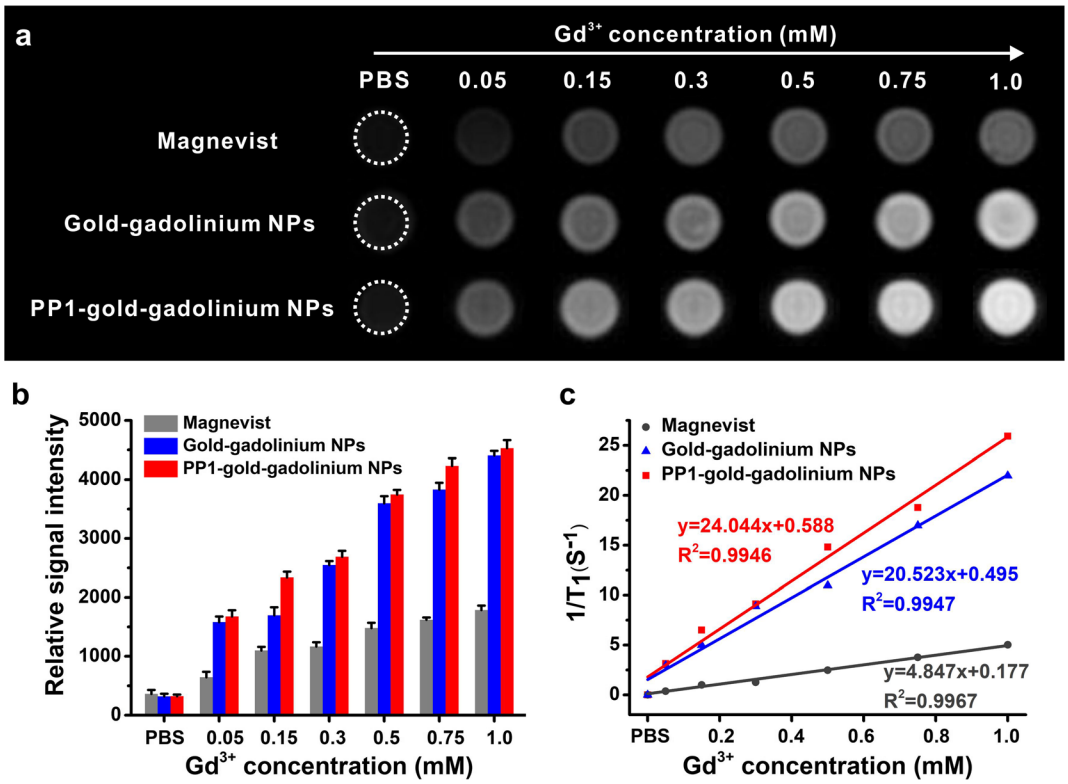

Fig. 2 In vitro MRI of the NPs. **a** T1-weighted MR contrast images and **b** corresponding MR signal enhancements (compared to PBS) of Magnevist, gold-gadolinium NPs and PP1-gold-gadolinium NPs. **c** Linear fitting of 1/T1 values as a function of Gd concentration

T1 contrast effect. This comparative study demonstrated superior relaxation properties of nano-sized PP1-gold-gadolinium NPs over their small Gd^{3+} counterparts, acting as high-performance T1-positive contrast agents for biomedical imaging.

Stability and biocompatibility study

Prior to in vivo applications, the stability of PP1-gold-gadolinium NPs was carefully investigated after incubation with different solutions including DI water, PBS (0.01 M, pH 7.4), and DMEM (10% FBS) over 10 weeks. As summarized in Fig. S7, storage of PP1-gold-gadolinium NP solution at room temperature under ambient conditions for 10 weeks did not obviously change their physiognomy or cause macroscopic precipitation. The HDs and zeta potentials were monitored as key criteria to estimate the colloidal stability (Wu et al. 2018a, b), which remained almost unchanged within the observation time (Fig. S8a-b). Moreover, MR signal intensities and longitudinal relaxation times (T1) of PP1-gold-gadolinium NPs were characterized in Fig. S8c-d, which were almost intact as well, suggesting good structural stability. Taken together, these results demonstrated outstanding stability of PP1-gold-gadolinium NPs in physiological circumstances, which might be attributed to the GSH coating shell, a very stable protein under different conditions (Yang et al. 2016).

Furthermore, the biocompatibility of the as-prepared PP1-gold-gadolinium NPs was evaluated in RAW264.7 and 293 T cell lines using MTT assay. After incubation of the cells with different concentrations of the NPs for 24 h, no obvious cytotoxicity was observed (Fig. S9a-b). The relative cell viability was maintained up to 82% even after incubation for 48 h at the highest concentration of 600 μg/mL (Fig. S9c-d), demonstrating that the toxic Gd^{3+} ions were not released from PP1-gold-gadolinium NPs under the experimental conditions (Wu et al. 2018a, b). This promising biocompatibility of PP1-gold-gadolinium NPs profited from the biocompatible synthesis route and GSH encapsulation, which suggested their significant potential for further in vivo molecular imaging.

Cellular binding specificity of PP1-gold-gadolinium NPs

Firstly, laser scanning confocal microscopy was utilized to observe the cellular binding specificity of the PP1-gold-gadolinium NPs. In this study, Cy5 was attached to the NP surfaces for fluorescence imaging. Human Ox-LDL-activated RAW264.7 macrophages were used as in vitro inflammatory model of foam cells (Wen et al. 2014). In comparison with control macrophages without pre-activation of human Ox-LDL (Fig. S10), the Ox-LDL-treated RAW264.7 cells exhibited much stronger red fluorescence in the targeted NPs group (Fig. 3), indicating PP1-gold-gadolinium NPs were generously internalized into activated RAW264.7 macrophages within 4 h. In sharp contrast, incubating with untargeted gold-gadolinium NPs, the red fluorescence on the surface of both non-activated and activated macrophages were almost absent. To further verify the specificity of PP1-gold-gadolinium NPs to activated RAW264.7 cells, we preincubated RAW264.7 cells with excess PP1 at 37 °C for 2 h. Results in Fig. 3 revealed that the fluorescence signal was conspicuously suppressed in the competitive inhibition group, because free PP1 antibody competitively bound to antigen in the preincubation stage, leading to a reduced binding rate of PP1-gold-gadolinium NPs to activated macrophages. These results suggested that the distinct red fluorescence of activated RAW264.7 cells from PP1-gold-gadolinium NPs was exactly through specific binding of PP1 antibody to the antigen SR-AI.

Since PP1-gold-gadolinium NPs exhibited a strong T1 enhancement effect, we next explored the potential of it to detect the activated RAW264.7 macrophages in vitro through targeted MR imaging. Consistent with confocal imaging, Fig. 4 a demonstrated the highest engulfment of PP1-gold-gadolinium NPs when macrophages were pre-exposed to human Ox-LDL.

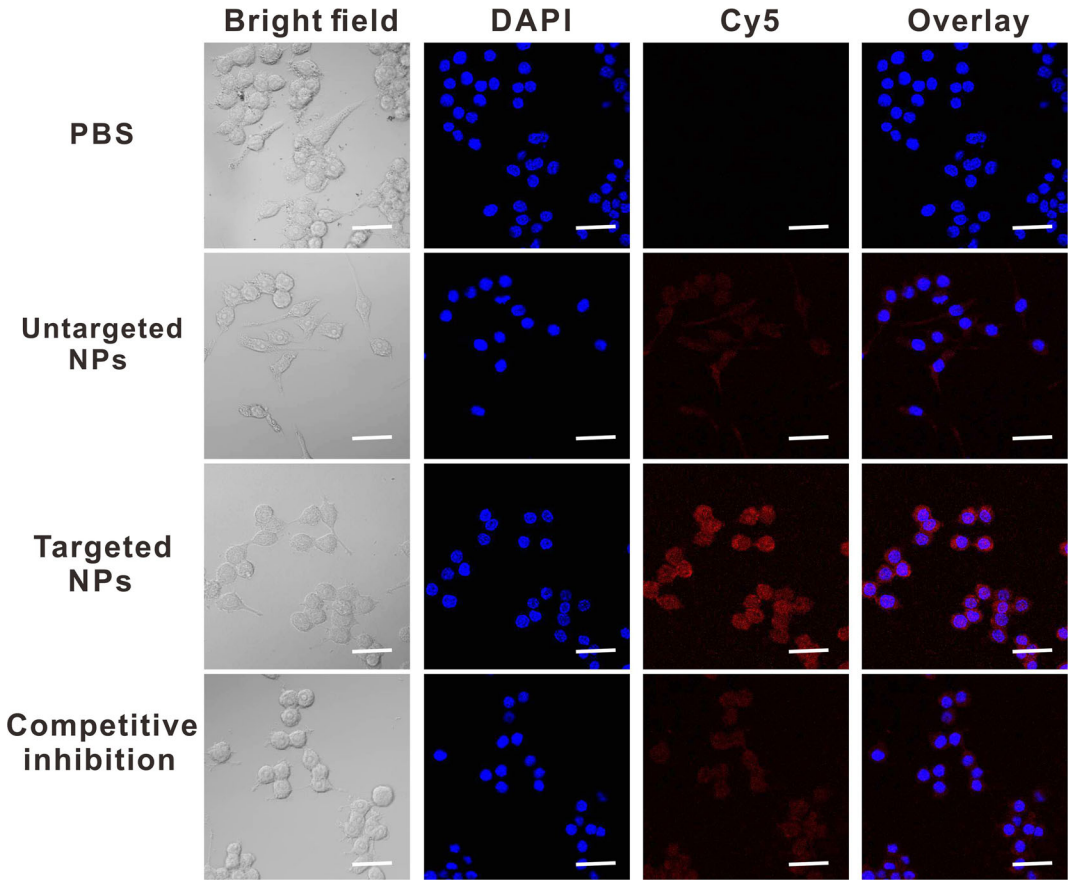

Fig. 3 Macrophage binding specificity. Confocal fluorescence images of RAW264.7 macrophages after incubation with PBS, gold-gadolinium NPs, PP1-gold-gadolinium NPs, and PP1-gold-gadolinium NPs plus excess free PP1 peptide (30 μg/mL) for 4 h, respectively. Macrophages were preincubated with human Ox-LDL for 24 h before NPs were added. Scale bar 10 μm

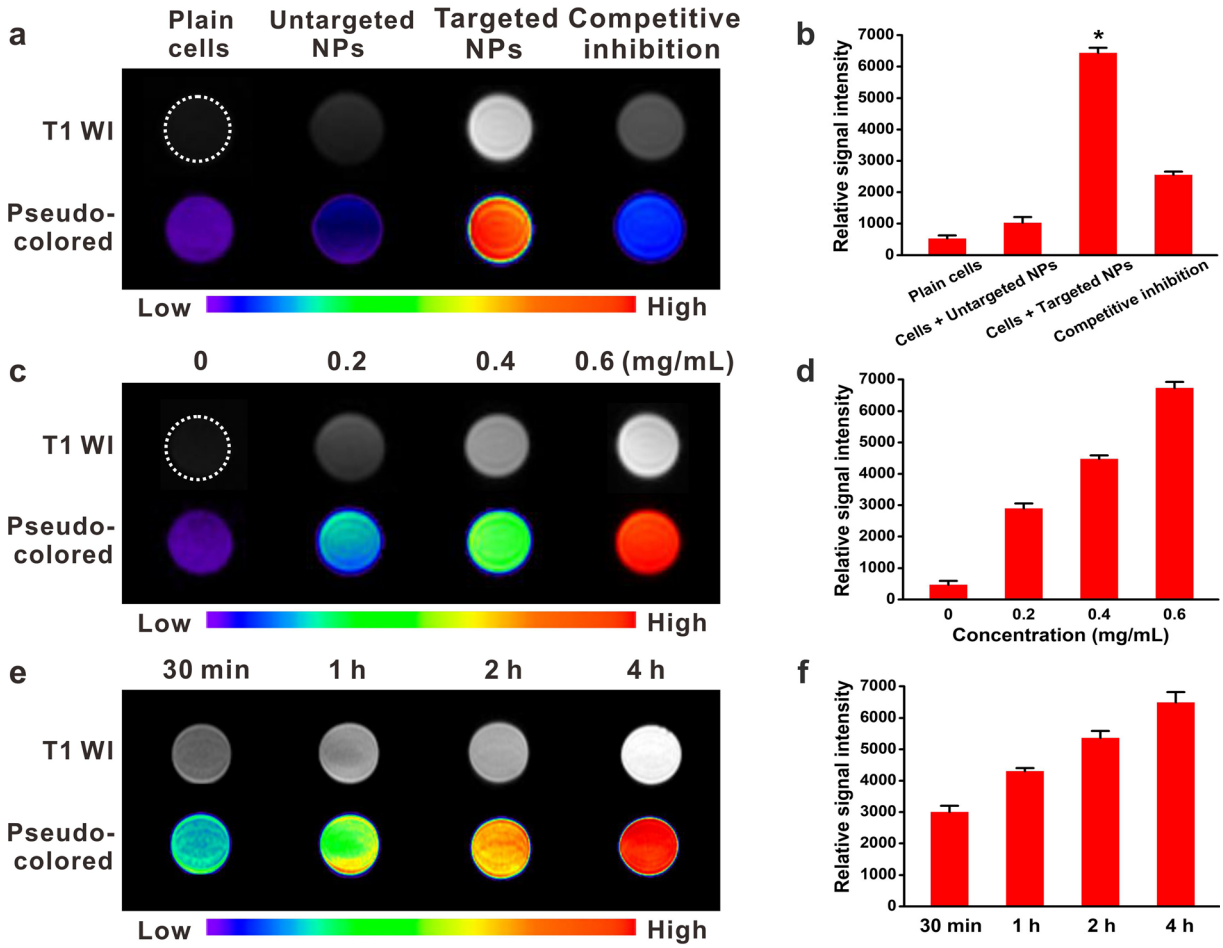

Fig. 4 MR imaging of RAW264.7 macrophage suspensions. **a** T1-weighted MR, pseudo-color images, and **b** relative signal intensities of activated macrophages incubated with PBS, gold-gadolinium NPs, PP1-gold-gadolinium NPs, and PP1-gold-gadolinium NPs plus free PP1 peptide for 4 h. **c** T1-weighted MRI and **d** relative signal intensities of activated macrophages incubated with PP1-gold-gadolinium NPs at different concentrations. **e** T1-weighted MRI and **f** relative signal intensities of activated macrophages after variable incubation time with PP1-gold-gadolinium NPs

Quantification of relative MR signal intensities precisely indicated that cellular internalization of gold-gadolinium NPs and PP1-gold-gadolinium NPs was 1028 ± 179 and 6436 ± 161, respectively, and it was eliminated to 2557 ± 100 after inhibition by free PP1 peptide ($p < 0.05$, Fig. 4b). In addition, the internalization of PP1-gold-gadolinium NPs was very limited in non-activated macrophages without pre-exposure to human Ox-LDL (Fig. S11). Figure 5 c and d display the relative MR signal intensities of activated RAW264.7 macrophages treated with various concentrations of PP1-gold-gadolinium NPs, which exhibited concentration-dependent and time-dependent MR signal augmentation. As a comparison, there were negligible signal increasement when macrophages were treated with Magnevist at the same Gd concentrations after the corresponding incubation times (Fig. S12). These observations powerfully suggested that PP1-gold-gadolinium NPs could specifically target SR-AI via PP1 antibody; hence, it was a promising selective positive MR imaging contrast agent for detecting activated macrophages in vitro.

In vivo MR imaging

Figure 6 summarizes representative in vivo T1-weighted MR images of the carotid arteries of ApoE$^{-/-}$ mice obtained pre-, 4 h, and 12 h following the administration of different nanoparticles at a dose of 200 mg/kg (0.2 mmol Gd/kg body weight). A significant

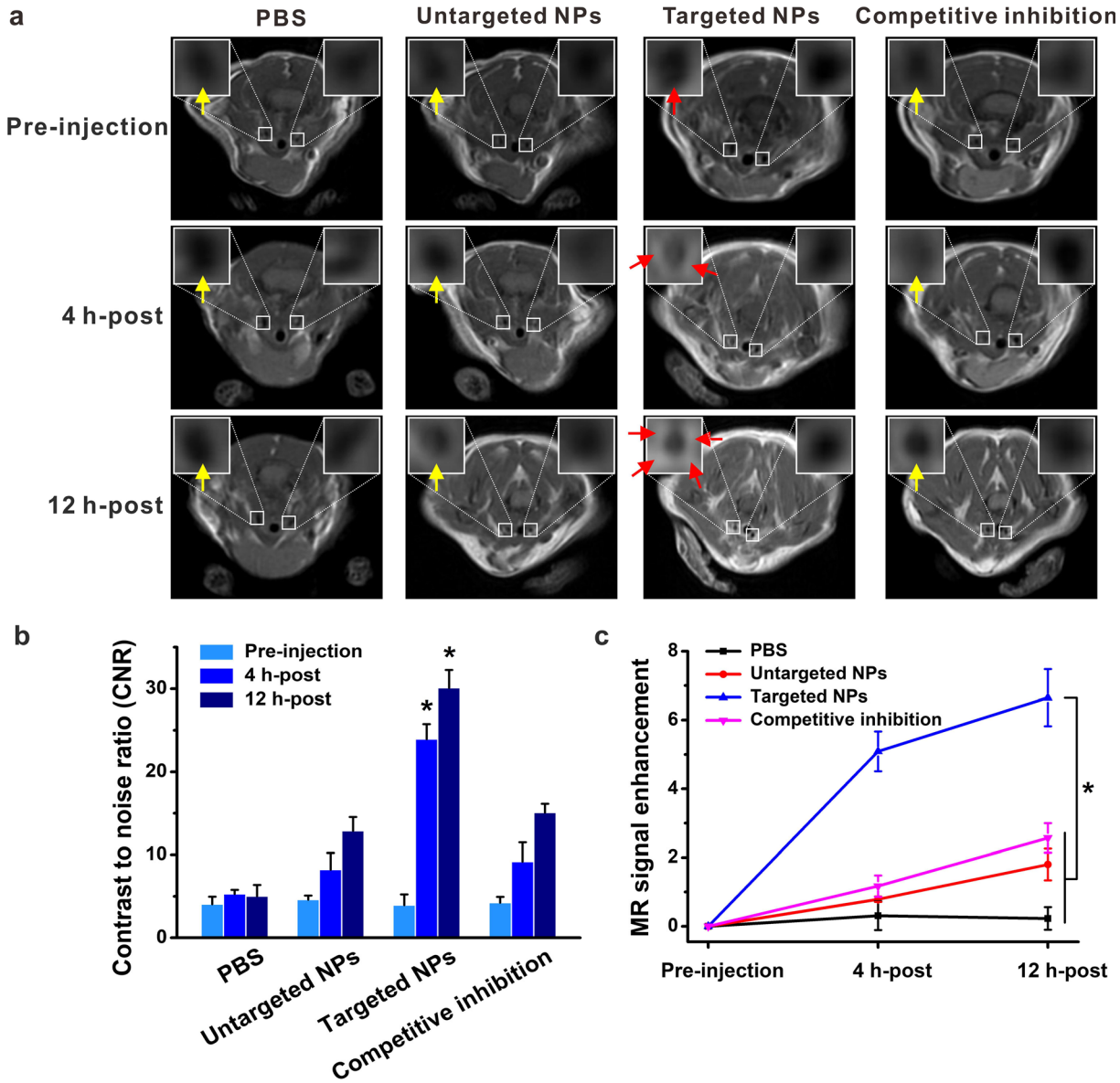

Fig. 5 In vivo MRI of ApoE$^{-/-}$ mice with different nanoparticles. **a** Representative in vivo MR images of the carotid arteries in ApoE$^{-/-}$ mice obtained pre-, 4 h, and 12 h after administration of various NPs (the arrows indicate the cross section of the left carotid atherosclerotic lesions). **b** Histogram showing a significant increase in CNR in the PP1-gold-gadolinium NP group. **c** Relative MR signal intensity changes in the left carotid atherosclerotic lesions of ApoE$^{-/-}$ mice among different groups

signal augmentation in the left carotid atherosclerotic lesions was observed at 4 h and 12 h following PP1-gold-gadolinium NPs administration (red arrows, Fig. 5a), and the pronounced accumulation of NPs was confirmed by the subsequent silver-staining (Fig. 6). The CNR values were calculated as 23.94 ± 1.80 and 30.10 ± 2.16, and the relative signal enhancements were 5.09 ± 0.58 and 6.65 ± 0.83 for 4 h and 12 h post-PP1-gold-gadolinium NP injection (Fig. 5b, c). This sustaining signal increasing demonstrated superior penetration and retention behavior in plaques of the PP1-gold-gadolinium NPs, which was mainly attributed to GSH shell and PP1 modification, helping them in blood escape RES capture and strengthen targeting efficiency to atherosclerotic lesion sites. Instead, the simultaneous administration of sufficient free PP1 with PP1-gold-gadolinium NPs prominently inhibited the changes in CNR (9.18 ± 2.33 and 15.08 ± 1.06) and relative signal

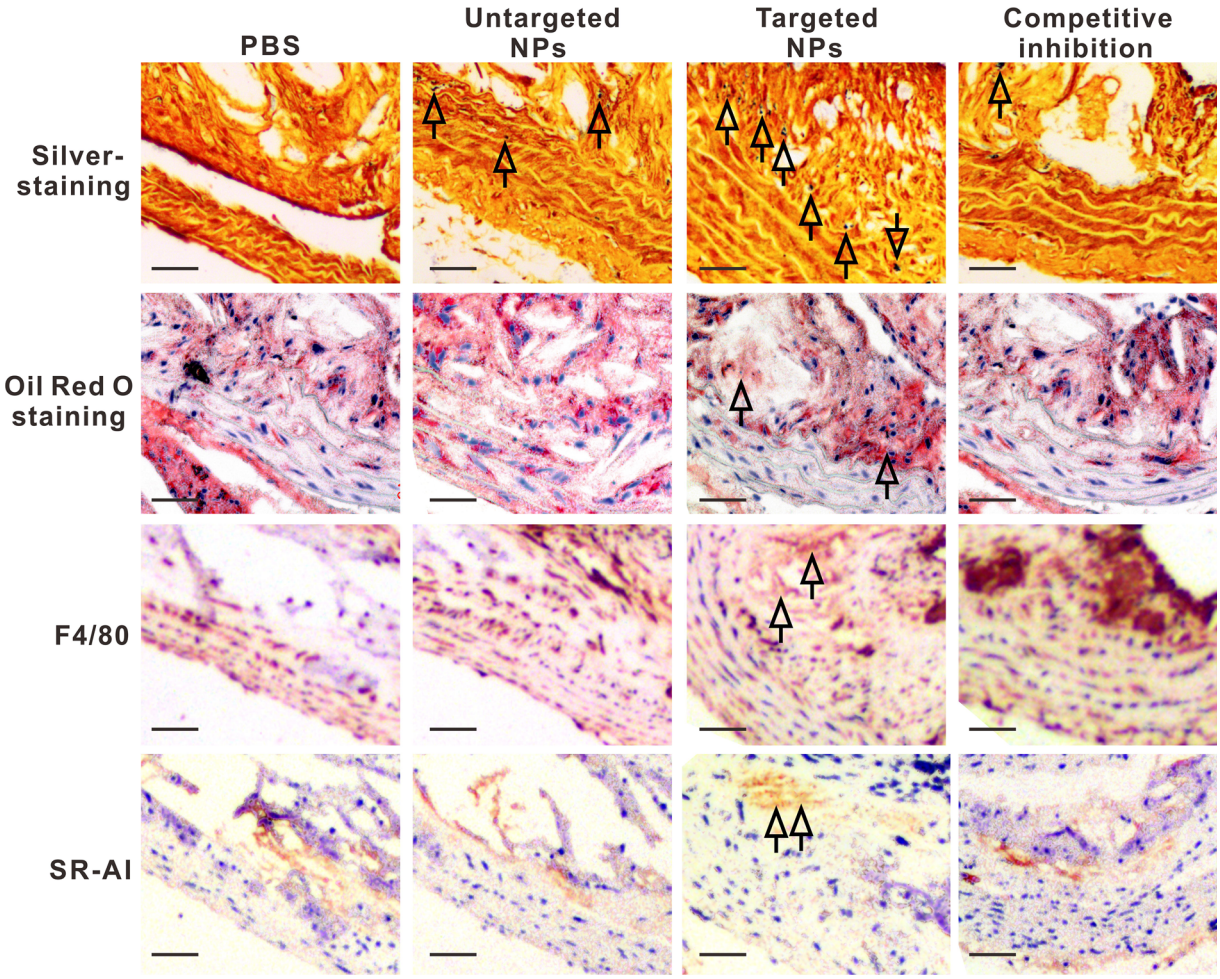

Fig. 6 Histomorphometry and immunohistochemistry of the left carotid atherosclerotic lesions of ApoE$^{-/-}$ mice administrated with various NPs. The left carotid artery sections were stained for NPs (silver-staining), lipids (Oil Red O staining), macrophages (F4/80), and SR-AI. Arrows indicate the location of NPs deposition while lipids, macrophages, and SR-AI are high expressed in the targeted NPs group. Bar = 50 μm

enhancements (1.17 ± 0.31 and 2.57 ± 0.43) at 4-h and 12-h post-injection. Untargeted gold-gadolinium NPs presented depressed CNR of 8.22 ± 2.00 and 12.87 ± 1.68 and limited signal changes of 0.79 ± 0.08 and 1.80 ± 0.46, respectively. Furthermore, barely discernible MR signal improvement was observed in the left carotid atherosclerotic lesions in the Magnevist-injected mice (Figure S13), due to the lack of tissue specificity and low relaxation time of the commercial Magnevist.

Histomorphological and immunohistochemical analysis

After in vivo imaging, histological examinations were immediately conducted to verify the signal enhancements in these regions and to explore interactions among the NPs, lipids, macrophages, and SR-AI within atherosclerotic carotid lesions. Microscopy images of consecutive carotid sections executed for silver-staining, Oil Red O staining, and immunohistochemical staining of F4/80 and SR-AI revealed marked aggregation of PP1-gold-gadolinium NPs in the intimal hyperplasia areas of left carotid atherosclerotic plaques, which primarily consisted of numerous F4/80-positive macrophages (Fig. 6), confirming the extensive engulfment of PP1-gold-gadolinium NPs by SR-AI enriched foam macrophages. On the contrary, even with SR-AI/macrophages (F4/80)/lipids abundant, there was limited NP deposition in the left carotid atherosclerotic lesions in untargeted gadolinium NP group and the competitive inhibition group. As a comparison, there was negligible

signal change after PP1-gold-gadolinium NP administration in the normal right carotid arteries of ApoE$^{-/-}$ mice (Fig. S14). Histological staining showed minimal NP deposition in the healthy right carotid arteries, where the SR-AI, macrophages, and lipids were practically absent (Fig. S15). These pathological analyses confirmed the active targeting efficacy of PP1-gold-gadolinium NPs to SR-AI over-expressed foam macrophages and the feasibility of it to quantitatively evaluating atherosclerotic lesions in vivo.

Pharmacokinetic, biodistribution, and bioelimination of PP1-gold-gadolinium NPs

In order to ensure biosafety for further clinical translation, it is important to evaluate the bioclearance and metabolism of nanoparticles after systemic administration. Here, we assessed the in vivo pharmacokinetics of gadolinium and gold in the serial blood samples at various time points after intravenous injection of PP1-gold-gadolinium NPs via ICP-MS. As shown in Fig. S16a-b, the blood circulation behaviors of both metal elements were exactly conformed to biexponential models with the elimination half-lives of around 5.42 h and 4.28 h, respectively. This time course profile could be ascribed to the GSH shell protection and PP1 targeting peptide (Yang et al. 2016), which might help PP1-gold-gadolinium NPs in blood strength EPR effect and deposit in atherosclerotic lesion sites.

Simultaneously, the dynamic metal content transformation of metabolic organs was carefully monitored to provide a real-time visualization of PP1-gold-gadolinium NPs metabolism. At 24 h, 3 days, and 7 days after PP1-gold-gadolinium NP administration, we collected major organs and excrements from mice including the heart, liver, spleen, lung, kidney, stomach, intestine, muscle, fat, bone marrow, lymph, bile, feces, and urine, and analyzed for ICP-MS. The gadolinium content analysis revealed the substantial presence in urine, bile, and feces after 24 h (Fig. S16c), demonstrating that most of the gadolinium was excreted out of the body through the renal system and the hepatobiliary system. Another portion of gadolinium was found in kidney for 24-h post-injection, indicating it could penetrate the kidney tissue to be metabolized (Zhang et al. 2012) thanks to its appropriate solubility, size, and surface charge (Longmire et al. 2008). Meanwhile, gold was predominantly excreted into bile and eliminated through feces, with a fraction of it by renal clearance (Fig. S16d). More significantly, compared to iron-based particles by Segers et al. 2013 and Wang et al. 2016a, b, at 24-h post-injection, low residual levels of metals remained in the liver and spleen, key organs of the monocyte phagocytic system (RES). On day 3, a clear decrease of the metal contents was observed and on day 7, the metal concentrations in all major organs were nearly nondetectable. These biodistribution-bioelimination data illustrated the exogenous metals had a quite short residence time in vivo, providing empirical evidence to substantiate excellent pharmacokinetics of PP1-gold-gadolinium NPs.

In vivo toxicology analysis

In order to investigate the toxicity of PP1-gold-gadolinium NPs in vivo, body weight, serum biochemistry, complete blood cell count, and histological changes were successively evaluated. Figure S17a gave the body weight of mice treated by PBS and the NPs. It can be seen that the treatment with PP1-gold-gadolinium NPs at a dosage of 200 mg/kg did not cause mortality or obvious adverse effects on growth compared to the control group within a 30-day observation period. Further, no abnormal clinical signs or behaviors were detected in both control and NP-treated groups.

For the blood biochemistry test, we focused on eight essential hepatorenal function indicators (Kheirolomoom et al. 2015), such as total protein (TP), alanine albumin (ALB), aspartate alkaline phosphatase (ALP), aminotransferase (ALT), aminotransferase (AST), total bilirubin (TBIL), creatinine (CREA), and blood urea nitrogen (BUN). As displayed in Fig. S17b, no significant difference in the levels of these markers between the treatment and control groups was observed during 30 days, indicating good liver and kidney safety profile of PP1-gold-gadolinium NPs. Concurrently, we selected standard hematology parameters for analysis, including white blood cells (WBC), red blood cells (RBC), platelets (PLT), hemoglobin (HGB), hematocrit (HCT), mean corpuscular volume (MCV), mean corpuscular hemoglobin (MCH), and mean corpuscular hemoglobin concentration (MCHC). Hematological results presented in Fig. S18 revealed that all of these markers were within normal range after 24-h treatment, and there was negligible difference from the control mice, indicating good hemocompatibility of PP1-gold-gadolinium NPs.

Finally, the potential long-term in vivo toxicity which may be caused by PP1-gold-gadolinium NPs was checked by assessing histological changes in several susceptible organs, including heart, liver, spleen, lungs, and kidneys. As shown in Fig. S19, compared with PBS-injected mice, there were no macroscopic pathological lesions in major organs of PP1-gold-gadolinium NP-injected mice. No appreciable inflammatory infiltrate or cell necrosis was observed in major organs after 14 days. These results clearly confirmed that PP1-gold-gadolinium NPs had good biosafety, which is crucial for further biomedical applications.

Conclusions

In summary, we have successfully fabricated foam macrophage targeting, biocompatible and biodegradable PP1-gold-gadolinium NPs via a facile, one-pot, environmentally benign and reproducible protocol. The as-prepared PP1-gold-gadolinium NPs exhibited pronounced T1-weighted MR contrast capability with good stability, which could provide important information for noninvasively characterizing vulnerable atherosclerotic lesions. More significantly, PP1-gold-gadolinium NPs retained the high paramagnetic property of Gd and inherent biological functions of PP1 within a single nanoplatform, thus demonstrating unique advantages over conventional nanoparticles such as enhanced T1 MR signal amplification and selective and precise atherosclerosis localization in vivo. In addition, this protein-based MRI contrast agents were efficiently cleared by renal and hepatobiliary systems and no observable toxicity or side effects were found either in vitro or in vivo. These results suggest that PP1-gold-gadolinium NPs offers an effective, safer candidate for clinical implementation for activated and sensitive MR detection of atherosclerosis and opens up the possibility of MR imaging-guided delivery vehicle for a wide range of theranostic applications.

Funding This study was funded by the National Natural Science Foundation of China (81701826), Key Project of Tianjin Natural Science Foundation (16KPXMSF00140), Key Project of Tianjin Health and Family Planning Commission (16KG115), and Science Foundation of the Second Hospital of Tianjin Medical University (2017YDEY11, 2018YDEY11).

Compliance with ethical standards

Conflict of interest The authors declare that they have no conflict of interest.

References

Caravan P, Ellison JJ, McMurry TJ, Lauffer RB (1999) Gadolinium(III) chelates as MRI contrast agents: structure, dynamics, and applications. Chem Rev 99:2293–2352

Chen N, Wang H, Huang Q, Li J, Yan J (2014) Long-term effects of nanoparticles on nutrition and metabolism. Small 10: 3603–3611

Choi HS, Liu W, Misra P, Tanaka E, Zimmer JP, Ipe BI, Bawendi MG, Frangioni JV (2007) Renal clearance of nanoparticles. Nat Biotechnol 25:1165–1170

Deng S, Zhang W, Zhang B, Hong R, Chen Q, Dong J, Chen Y, Chen Z, Wu Y (2015) Radiolabeled cyclic arginine-glycine-aspartic (RGD)-conjugated iron oxide nanoparticles as single-photon emission computed tomography (SPECT) and magnetic resonance imaging (MRI) dual-modality agents for imaging of breast cancer. J Nanopart Res 17:19

Dweck MR, Aikawa E, Newby DE, Tarkin JM, Rudd JHF, Narula J, Fayad ZA (2016) Non-invasive molecular imaging of disease activity in atherosclerosis. Circ Res 119:330–340

Fuster V, Moreno PR, Fayad ZA, Corti R, Badimon JJ (2005) Atherothrombosis and high-risk plaque: part I: evolving concepts. J Am Coll Cardiol 46:937–954

Gough PJ, Greaves DR, Suzuki H, Hakkinen T, Hiltunen MO, Turunen M, Herttuala SY, Kodama T, Gordon S (1999) Analysis of macrophage Scavenger receptor (SR-A) expression in human aortic atherosclerotic lesions. Arterioscler Thromb Vasc Biol 19:461–471

Hiltunen TP, Luoma JS, Nikkari T, Ylä-Herttuala S (1998) Expression of LDL receptor, VLDL receptor, LDL receptor-related protein, and Scavenger receptor in rabbit atherosclerotic lesions: marked induction of scavenger receptor and VLDL receptor expression during lesion development. Circulation 97:1079–1086

Htun NM, Chen YC, Lim B, Schiller T, Maghzal GJ, Huang AL (2017) Near-infrared autofluorescence induced by intraplaque hemorrhage and heme degradation as marker for high-risk atherosclerotic plaques. Nat Commun 8:75

Hu D, Sheng Z, Zhang P, Yang D, Liu S, Gong P, Gao D, Fang S, Ma Y, Cai L (2013) Hybrid gold-gadolinium nanoclusters for tumor-targeted NIRF/CT/MRI triple-modal imaging in vivo. Nanoscale 5:1624–1628

Kheirolomoom A, Kim CW, Seo JW, Kumar S, Son DJ, Gagnon KJ, Ingham ES, Ferrara KW, Jo H (2015) Multifunctional nanoparticles facilitate molecular targeting and miRNA delivery to inhibit atherosclerosis in ApoE$^{-/-}$ mice. ACS Nano 9: 8885–8897

Kodama T, Freeman M, Rohrer L, Zabrecky J, Matsudaira P, Krieger M (1990) Type 1 macrophage scavenger receptor contains alpha-hehcal and collagen-like coiled coils. Nature 343:531–535

Kolodgie FD, Gold HK, Burke AP, Fowler DR, Kruth HS, Weber DK, Farb A, Guerrero LJ, Hayase M, Kutys R, Narula J, Finn AV, Virmani R (2003) Intraplaque hemorrhage and progression of coronary atheroma. N Engl J Med 349:2316–2325

Le W, Cui S, Chen X, Zhu H, Chen B, Cui Z (2016) Facile synthesis of Gd-functionalized gold nanoclusters as potential MRI/CT contrast agents. Nanomaterials 6:65

Longmire M, Choyke PL, Kobayashi H (2008) Clearance properties of nano-sized particles and molecules as imaging agents: considerations and caveats. Nanomedicine 3:703–717

Luo Z, Yuan X, Yu Y, Zhang Q, Leong DT, Lee JY, Xie J (2012) From aggregation-induced emission of Au(I)-thiolate complexes to ultrabright Au(0)@Au(I)-thiolate core-shell nanoclusters. J Am Chem Soc 134:16662–16670

McDonald RJ, McDonald JS, Kallmes DF, Jentoft ME, Murray DL, Thielen KR, Williamson EE, Eckel L (2015) Intracranial gadolinium deposition after contrast-enhanced MR imaging. Radiology 275:772–782

Nabel EG, Braunwald E (2012) A tale of coronary artery disease and myocardial infarction. N Engl J Med 366:54–63

Qiao R, Qiao H, Zhang Y, Wang Y, Chi C, Tian J, Zhang L, Cao F, Gao M (2017) Molecular imaging of vulnerable atherosclerotic plaques in vivo with osteopontin-specific upconversion nanoprobes. ACS Nano 11:1816–1825

Ross R (1999) Atherosclerosis - an inflammatory disease. N Engl J Med 340:115–126

Samira R, Hossein R, Mohammad HB, Shahram A (2011) MRI contrast agent for molecular imaging of the HER2/neu receptor using targeted magnetic nanoparticles. J Nanopart Res 13: 2285–2293

Segers FM, den Adel B, Bot I, van Graaf LM, Veer EP, Gonzalez W, Raynal I, de Winther M, Wodzig WK, Poelmann RE, van Berkel TJ, van Weerd L, Biessen EA (2013) Scavenger receptor-AI-targeted iron oxide nanoparticles for in vivo MRI detection of atherosclerotic lesions. Arterioscler Thromb Vasc Biol 33:1812–1819

Segers FM, Yu H, Molenaar TJ, Prince P, Tanaka T, van Berkel TJ, Biessen EA (2012) Design and validation of a specific scavenger receptor class AI binding peptide for targeting the inflammatory atherosclerotic plaque. Arterioscler Thromb Vasc Biol 32:971–978

Arbab-Zadeh A, Nakano M, Virmani R, FusterV (2012) Acute coronary events. Circulation 125:1147-1156

Suzuki H, Kurihara Y, Takeya M, Kamada N, Kataoka M, Jishage K, Ueda O, Sakaguchi H, Higashi T, Suzuki T, Takashima Y, Kawabe Y, Cynshi O, Wada Y, Honda M, Kurihara H, Aburatani H, Doi T, Matsumoto A, Azuma S, Noda T, Toyoda Y, Itakura H, Yazaki Y, Horiushi S, Takahashi K, Kruijt JK, Berkel TJ, Steinbrecher UP, Ishibashi S, Maeda N, Gordon S, Kodama T (1997) A role for macrophage scavenger receptors in atherosclerosis and susceptibility to infection. Nature 386:292–296

Virmani R, Burke AP, Farb A, Kolodgie FD (2006) Pathology of the vulnerable plaque. J Am Coll Cardiol 47:C13–C18

Wang J, Liu J, Liu Y, Wang L, Cao M, Ji Y, Wu X, Xu Y, Bai B, Miao Q, Chen C, Zhao Y (2016b) Gd-hybridized plasmonic Au-nanocomposites enhanced tumor-interior drug permeability in multimodal imaging-guided therapy. Adv Mater 28:8950–8958

Wang Y, Chen J, Yang B, Qiao H, Gao L, Su T, Ma S, Zhang X, Li X, Liu G, Cao J, Chen X, Chen Y, Cao F (2016a) In vivo MR and fluorescence dual-modality imaging of atherosclerosis characteristics in mice using profilin-1 targeted magnetic nanoparticles. Theranostics 68:272–286

Wen S, Liu D, Cui Y, Harris SS, Chen Y, Li KC, Ju S, Teng G (2014) In vivo MRI detection of carotid atherosclerotic lesions and kidney inflammation in ApoE-deficient mice by using LOX-1 targeted iron nanoparticles. Nanomedicine 10: 639–649

Winther MP, Van Dijk KW, Havekes LM, Hofker MH (2000) Macrophage scavenger receptor class A: a multifunctional receptor in atherosclerosis. Arterioscler Thromb Vasc Biol 20:290–297

Wu M, Zhang Y, Zhang Y, Wu M, Wu M, Wu H, Cao L, Li L, Li X, Zhang X (2018b) Tumor angiogenesis targeting and imaging using gold nanoparticle probe with directly conjugated cyclic NGR. RSC Adv 8:1706–1716

Wu T, Chen X, Wang Y, Xiao H, Peng Y, Lin L, Xia W, Long M, Tao J, Shuai X (2018a) Aortic plaque-targeted andrographolide delivery with oxidation-sensitive micelle effectively treats atherosclerosis via simultaneous ROS capture and anti-inflammation. Nanomedicine 14:2215–2226

Yan F, Sun Y, Mao Y, Wu M, Deng Z, Li S, Liu X, Xue L, Zheng H (2018) Ultrasound molecular imaging of atherosclerosis for early diagnosis and therapeutic evaluation through leucocyte-like multiple targeted microbubbles. Theranostics 8:1879–1891

Yang W, Guo W, Le W, Lv G, Zhang F, Shi L, Wang X, Wang J, Wang S, Chang J, Zhang B (2016) Albumin-bioinspired Gd: CuS nanotheranostic agent for in vivo photoacoustic/magnetic resonance imaging-guided tumor-targeted photothermal therapy. ACS Nano 10:10245–10257

Yu M, Zhou C, Liu L, Zhang S, Sun S, Hankins JD, Sun X, Zheng J (2017) Interactions of renal-clearable gold nanoparticles with tumor microenvironments: vasculature and acidity effects. Angew Chem Int Ed 56:4314–4319

Zhang S, Zou L, Zhang D, Pang X, Yang H, Xu Y (2011) GoldMag nanoparticles with core/shell structure: characterization and application in MR molecular imaging. J Nanopart Res 13:3867–3876

Zhang X, Wu D, Shen X, Liu P, Fan F, Fan S (2012) In vivo renal clearance, biodistribution, toxicity of gold nanoclusters. Biomaterials 33:4628–4638

Zhao Y, Peng J, Li J, Huang L, Yang J, Huang K, Li H, Jiang N, Zheng S, Zhang X, Niu Y, Han G (2017) Tumor-targeted and clearable human protein-based MRI nanoprobes. Nano Lett 8:28

Zhou Z, Qutaish M, Han Z, Schur RM, Liu Y, Wilson DL, Lu Z (2015) MRI detection of breast cancer micrometastases with a fibronectin-targeting contrast agent. Nat Commun 6:7984